Rapid Communications

Rupture time of droplets impacted by a burst of picosecond laser pulses

Duane Hudgins and Reza S. Abhari*
Laboratory for Energy Conversion, ETH Zurich, Sonneggstrasse 3, 8092 Zurich, Switzerland

(Received 18 September 2018; revised manuscript received 6 March 2019; published 29 March 2019)

Liquid Sn droplets were irradiated with shaped bursts of picosecond laser pulses. The shapes of the deforming droplets following the impact of the recoil pressure induced by these bursts were imaged using a high-speed shadowgraph system. The rupture time $\tilde{t}_b$ of the droplet expanding as a thin fluid film was measured for each case. A Rayleigh-Taylor instability analysis is done in order to determine the dependences governing $\tilde{t}_b$. The evidence supports the hypothesis that the initial perturbations of the developing Rayleigh-Taylor instabilities are on the order of the ablation depth and that there is a lower cutoff wavelength of these initial perturbations of $\sim$10 μm.

DOI: 10.1103/PhysRevE.99.031102

I. INTRODUCTION

Droplet deformation and rupture by a pulsed laser impact has been of continuing interest over the past decade. A large contributor to this interest has been the development of droplet-based laser produced plasma (LPP) light sources with a focus on the generation of extreme ultraviolet (EUV) light [1,2]. A challenge with these systems is the generation neutral cluster debris, which are liquid droplet fragments ejected from the source during the generation of the laser plasma [3]. These neutral clusters can damage or coat sensitive optics and instruments within the source chamber [4]. In order to mitigate this damage, it is necessary to understand the dynamics of the droplet fragmentation. The process of fluid film perforation determines the neutral cluster size distribution and trajectory. When the impacted droplet expands either by accelerated surface rim expansion or by cavitation, the fluid deforms first as a stretching sheet. At a given time after the impact, holes form in the sheet that quickly expand and merge together forming ligaments that fragment into neutral clusters [5]. Some investigations into this phenomena have already been done by Klein [6] and Kurilovich *et al.* [7], where the rupture time is shown to have an exponential dependence on the impact Weber number. In this Rapid Communication, liquid Sn droplets are irradiated by picosecond laser bursts, with the bursts varying in the number of pulses and the energy distribution of the pulses within the bursts [8]. The deformation dynamics are observed using a high-speed shadowgraph imaging system, which images the deforming droplet shape at different times. A Rayleigh-Taylor instability analysis similar to that presented by Klein [6] is performed in order to predict the first hole appearance time, albeit with different assumptions. The model results present compelling evidence for the presence of a lower cutoff wavelength of the excited wave modes of the laser ablation accelerated surface of the droplet.

II. EXPERIMENTAL SETUP

The experiment was conducted within a vacuum chamber at 0.02 mbar with an Ar background gas (see Fig. 1). A droplet dispenser generates a monodispersed and coherent stream of droplets of liquid Sn. The droplet frequency is determined by a piezoelectric actuator and was operated between 20 and 33 kHz for the various cases. The droplet sizes typically vary between 30 and 100 μm. The droplet dispenser is mounted to a three-dimensional (3D) motion stage and coupled to a closed loop control system able to keep the position of the droplet train at the main laser focus position. The control system compensates for lateral instabilities with a spatial resolution of $\pm$0.5 μm [9]. The laser is a master oscillator power amplifier (MOPA) Nd-doped vanadate (Nd:VAN) system with a wavelength of 1064 nm. The master oscillator is a pulsed laser diode that generates pulses with a duration of $\tau_p = 43$ ps [full width at half maximum (FWHM)] that are amplified through several stages. It is capable of single-pulse to 100-MHz repetition rates with single-pulse energies up to $E_p \leqslant 2$ mJ. Using an acousto-optic modulator, the oscillator output is modulated in order shape bursts with energies up to $E_B \leqslant 2.7$ mJ. The laser spot was focused to a spot diameter of $\phi_f = 22$ μm (FWHM).

The deforming droplet was imaged using a high-speed shadowgraph system. The shadowgraph system consists of a high-speed camera (SONY ICX625ALA/AQA) capable of up to 20 fps. The image resolution was 0.93 μm/pixel. The flash is a high-powered light-emitting diode (LED) pulsed at 500-ns duration. The system trigger signals for the laser, camera, and flash are synchronized such that during the source operation the delays between these signals can be changed with 0.25-μs resolution.

In total, 34 unique burst interactions were imaged, with two or more pulses in a burst. For each case an average of five time steps were imaged and for each time step $\sim$100 images were acquired. Each image is a unique droplet impact. The radius of the expanding sheet $R(t)$ (see Fig. 2) was measured for these images and was found to vary with a maximum standard of deviation of 8% relative to the mean. Therefore, the images for

*rabhari@lec.mavt.ethz.ch

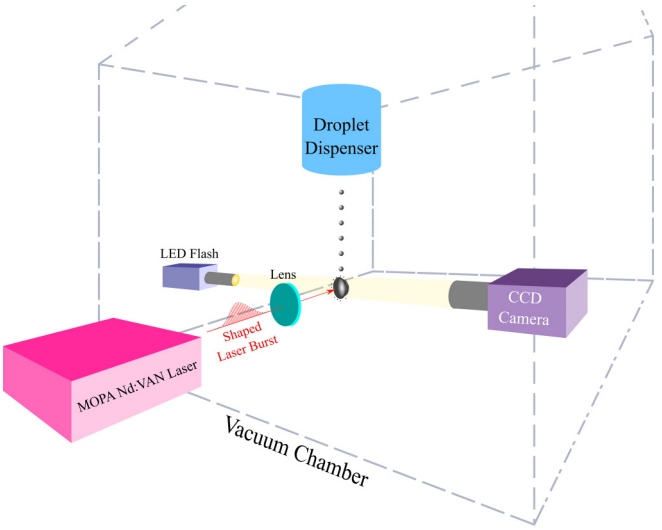

FIG. 1. The functional layout of the experiment. The deforming droplets were imaged at 90° relative to the laser axis.

each time step are considered highly repeatable with regards to the investigated parameters for this work, mainly sheet expansion rate and first hole appearance time.

For the investigated cases, the total burst energy E_B and the pulse energy E_p are made dimensionless relative to the initial surface energy as $\tilde{E}_B = E_B/(\sigma d_0^2)$ and $\tilde{E}_p = E_p/(\sigma d_0^2)$, where $\sigma = 0.55$ N/m is surface tension, d_0 is the original droplet diameter, and $\tilde{E}_B$ is varied from $\tilde{E}_B = 6.0 \times 10^4$ to 5.6×10^5. Throughout this work all of the length scales are made dimensionless (indicated by the tilde "∼" notation) with respect to the initial droplet radius r_0 and the timescales with the droplet capillary time $\tau_c = \sqrt{\rho r_0^3/\sigma}$, where ρ is the fluid density. The capillary timescales in this work are ∼30 μs. Examples of the burst shapes used for this work are shown in Figs. 3(a)–3(f).

Another key dimensionless parameter used in this work is a modified Weber number denoted as the splash Weber number We_s of the droplet impact defined as $\mathrm{We}_s = \rho d_0 u_0^2/\sigma$, where $\sim u_0$ is the peak initial droplet surface velocity after the acceleration by the laser burst [10]. The surface velocity decreases in magnitude away from the laser peak irradiation region [3,11]. We_s is measured for all cases using the function

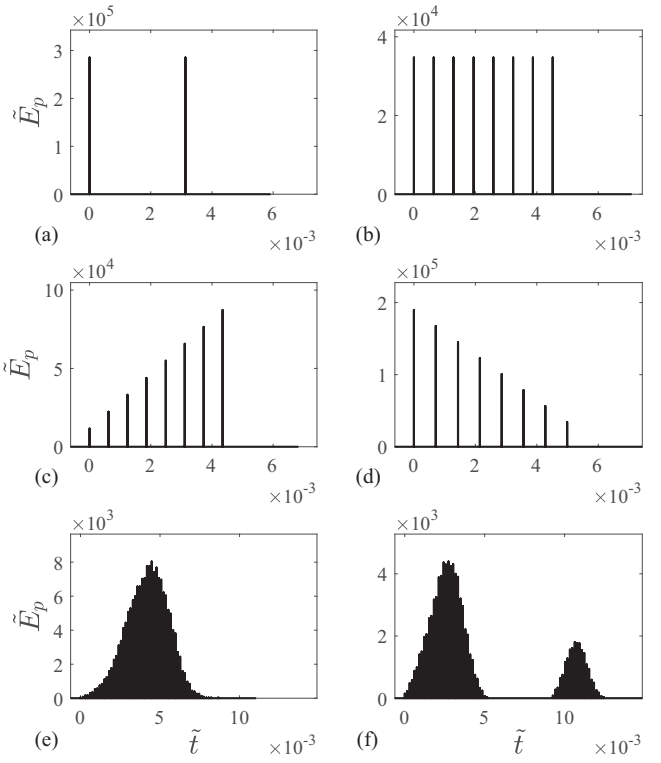

FIG. 3. Examples of burst profiles implemented in this work for (a) double pulse, (b) flattop (FT), (c) rising sawtooth (RST), (d) falling sawtooth (FST), (e) Gaussian, (f) double burst. Each peak represents one laser pulse of the shown dimensionless pulse energy $\tilde{E}_p$ at the time from the beginning of the burst $\tilde{t}$.

for an inviscid, incompressible, impacted droplet deforming in free space by Villermaux and Bossa [12],

$$\tilde{R}(\tilde{t}) = 1 + \sqrt{\frac{1}{2}\mathrm{We}_s}\,\tilde{t}\left(1 - \frac{\sqrt{3}}{2}\tilde{t}\right)^2. \quad (1)$$

By fitting the $\tilde{R}(\tilde{t})$ to Eq. (1) for data points before the expanding sheet is perforated, We_s is found for each case (see Fig. 4). One should note that $u_0 \approx \dot{R}(\tilde{t} \ll 0.39)$. The flow is considered inviscid by checking the Reynolds number $\mathrm{Re}_s = \rho d_0 u_0/\mu$, where μ is the dynamic viscosity of ∼0.001 05 Pa s

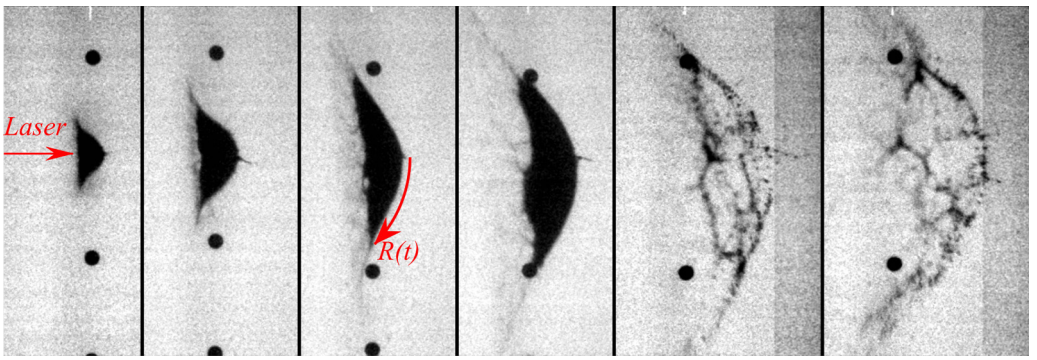

FIG. 2. An example sequence illustrating the rim expansion and sudden rupture of the expanding sheet into a web of ligaments [$N_p = 8$, $\tilde{E}_B = 2.4 \times 10^5$, 20 MHz, rising saw-tooth (RST) [see Fig. 3(c)]]. The timing from left to right is $\tilde{t} = 0.071$, 0.13, 0.20, 0.27, 0.41, and 0.59. The third frame displays $R(t)$, which is defined as the path length along the sheet from the sheet center to the rim.

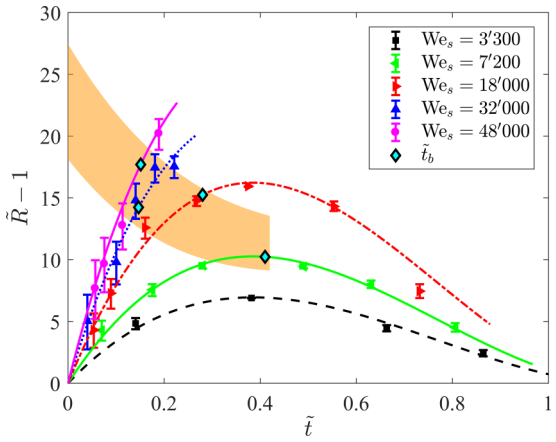

FIG. 4. Example cases of varying We$_s$. The markers represent the measured $R(t)$ and the dashed lines represent the corresponding fit of (1) to measure We$_s$. The perforation times $\tilde{t}_b$ for the plotted cases are also shown. The highlighted area marks the range where $\tilde{t}_b$ is observed across all measured cases.

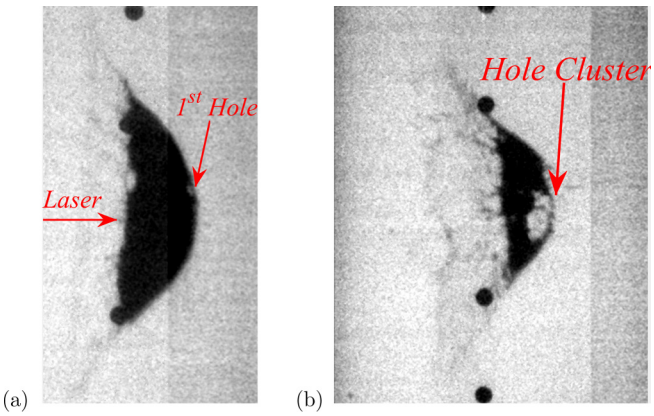

FIG. 5. Example cases showing first hole perforation, where (a) $N_p = 27$ and $\tilde{E}_B = 2.3 \times 10^5$, and (b) $N_p = 8$ and $\tilde{E}_B = 3.3 \times 10^5$.

[13]. Re$_s$ > 20′000 for the experimental cases and therefore the inviscid assumption is considered valid. The thickness of the expanding sheet h is approximated using conservation of mass and the rim radius from Eq. (1) as [12]

$$\tilde{h}(\tilde{t}) \sim \tfrac{4}{3}[\tilde{R}(\tilde{t})]^{-2}. \tag{2}$$

III. SHEET RUPTURE TIME

The observation of the experiments shows that after the droplet is impacted by the laser burst, the sheet expands into a thin liquid sheet. Depending upon the burst profile and energy the sheet will either expand to a maximum rim radius and then contract due to rim destabilization or the sheet will rupture during the rim evolution. When the sheet ruptures, a number of holes will perforate the sheet. The holes then expand, converting the sheet into a web of ligaments that break into fragments (Fig. 2). The time from the last pulse in the burst until the first hole appearance is defined as the breakup time t_b. For each case t_b is measured by identifying the earliest time when a hole appears on the sheet, as shown in Figs. 5(a) and 5(b). As seen in these figures, the holes can appear grouped together in clusters while other parts of the film remain unbroken. The measurement error in t_b includes shadowgraph exposure time and the estimate of the hole growth rate using Taylor-Culick as $t_{b,\mathrm{err}} = d_{h,\mathrm{err}}\sqrt{\rho\, h/(8\sigma)}$, where $d_{h,\mathrm{err}}$ is the uncertainty in the diameter of the observed first hole(s). In order to determine the rupture criteria for the expanding sheet, a similar approach to that done by Bremond and Villermaux [5] for a bursting fluid thin film is derived. This approach was further adapted for laser impacted droplets by Klein [6], which will be emulated in this work, except for some key differences in assumptions and formulation. The key differences lay in the formulation of the acceleration term a, the handling of the threshold time t_t for the thin sheet criteria, and the initial perturbation amplitude and wave-number range for a laser ablation accelerated target.

The sheet expansion is divided into three separate time phases. The first phase is for the time from $t = -\Delta t$ to the end of the burst $t = 0$, which is the duration of intermittent fluid acceleration. The second phase is the period before the droplet has flattened into the thin sheet $t = 0 \rightarrow t_t(k)$, where t_t is a function of the specific wave number k. The third phase is defined as the remaining time to the sheet rupture $t = t_t(k) \rightarrow t_b$, where t_b is denoted as the time for the first hole appearance in the droplet.

The modulations of the local surface waves on the droplet are represented as Fourier modes [5]

$$\tilde{\eta} = \tilde{\eta}_0 f(\tilde{t}) e^{i\tilde{k}\tilde{s}}, \tag{3}$$

where $\tilde{\eta}_0$ is the initial surface wave amplitude after the burst interaction, $\tilde{s}$ is the length coordinate tangent to the droplet surface, and $f(\tilde{t})$ is the evolution of the amplitude scale for the specific wave number $\tilde{k}$ as a function of time. Throughout this analysis $\tilde{k}$ refers to the wave number of the initial wave mode on the droplet surface before surface stretching occurs. Effects of stretching on $\tilde{k}$ will be compensated for in the model separately as explained further below.

There are two perturbation states that need to be determined for the initial conditions of phase 2, which are the wave-mode-dependent perturbation amplitude $\eta_0 = \eta(t = 0)$ and the perturbation growth rate $\dot{\eta}(t = 0)$. The initial perturbation amplitude is assumed to be on the order of the ablation depth. The ablation depth is expected to be in the range of $\eta_0 \sim$ 60–80 nm [14].

The initial growth rates for phase 2 are determined by approximating the intermittent laser driven acceleration as impulsive. Therefore the local acceleration of the droplet surface at the center of the radiating laser spot is approximated as $a \approx u_0/\Delta t = \mathrm{We}_s^{1/2}\, r_0/(\tau_c \Delta t)$, where Δt is the total duration of the acceleration period for the burst and $\Delta t \ll \tau_c$. The velocity scale u_0 was chosen for the Weber number since the surface in front of the laser spot will be accelerated to $\dot{R}(t = 0) \sim u_0$ [12,15]. The acceleration phase of the droplet is assumed to be impulsive with $\tilde{\omega}_{1,\mathrm{im}} \ll \Delta\tilde{t}^{-1}$, where $\tilde{\omega}_{1,\mathrm{im}}$ is the imaginary part of the wave mode growth rate $\tilde{\omega}_1$. The capillary wave number for the accelerated surface is defined as $\tilde{k}_c = \Delta\tilde{t}^{-1/2}\, \mathrm{We}_s^{1/4}$, which will determine the growth rates

of the wave modes of the first phase. Another phenomenon has been observed for laser ablation accelerated targets where there is a lower cutoff wavelength of $\lambda \sim 10\ \mu$m for surfaces accelerated with 1064-nm light due to the damping effects caused by the ablation [16,17]. This means there is a maximum wave number $\tilde{k}_{\max} = 2\pi/\lambda$ excited by the ablation driven acceleration. For the cases investigated, during the impulsive acceleration $\tilde{k}_c \gg \tilde{k}_{\max} \gg 1$ and the dispersion relation for the surface waves is given as [5]

$$\tilde{\omega}_1^2 = \left(\tilde{k}^3 - \tilde{k}_c^2\tilde{k}\right). \tag{4}$$

The initial conditions of the shape function $f(\tilde{t})$ in Eq. (3) are given such that [5]

$$f_1(\tilde{t}=0) = 1, \quad \dot{f}_1(\tilde{t}=0) = 0. \tag{5}$$

All shape function modes for $1 \leqslant \tilde{k} \leqslant \tilde{k}_{\max}$ start with the same initial amplitude and zero initial growth rate. The shape function $f_1(\tilde{t})$ is governed by [5]

$$\ddot{f}_1 = -\tilde{\omega}_1^2 f_1(\tilde{t}). \tag{6}$$

Using (4) and (5) the differential equation (6) is solved as

$$f_1(\tilde{t}) = \cos[\tilde{k}^{3/2}(\tilde{t}+\Delta\tilde{t})] + \frac{\mathrm{We}_s^{1/2}}{\tilde{k}^2\Delta\tilde{t}}\{1-\cos[\tilde{k}^{3/2}(\tilde{t}+\Delta\tilde{t})]\}, \tag{7}$$

$$\dot{f}_1(\tilde{t}) = -\tilde{k}^{3/2}\sin[\tilde{k}^{3/2}(\tilde{t}+\Delta\tilde{t})] + \frac{\mathrm{We}_s^{1/2}}{\tilde{k}^{1/2}\Delta\tilde{t}}\sin[\tilde{k}^{3/2}(\tilde{t}+\Delta\tilde{t})]. \tag{8}$$

Since the acceleration phase of the burst is treated as impulsive, the duration of phase 1 is approximated $\Delta\tilde{t} \to 0$ and the small angle approximation is used for the amplitude and growth rate. Therefore, the shape function at the end of phase 1 is given as $f_1(\tilde{t}=0) \approx 1$ and $\dot{f}_1(\tilde{t}=0) \approx \mathrm{We}_s^{1/2}\tilde{k}$. After the acceleration phase each surface wave mode will evolve, characteristic of an infinite medium where $\tilde{k}_c = 0$, until the flattening fluid film reaches the thin layer criteria $\tilde{k}\tilde{h} \ll 1$ [5]. Since $\tilde{h}$ is a function of time, each wave mode corresponding to $\tilde{k}$ will reach the flat sheet criteria at a different time denoted as $\tilde{t}_t$. The effect of the sheet surface expansion must be accounted for by self-similar stretching, since $\tilde{R} > 1$ for the wave modes already during phase 2. The stretching of the wave number is accounted for by dividing $\tilde{k}$ by $\tilde{R}$, giving a proportionate decrease in the wave number for an increase in the sheet length [18]. Therefore, t_t is the time that satisfies $\tilde{k}\tilde{R}^{-1}\tilde{h} = 1$ ($\tilde{R}^{-1}$ accounts for self-similar stretching), which by combining with (1) and (2) is

$$\tilde{t}_t \approx \left[\left(\frac{4}{3}\tilde{k}\right)^{1/3} - 1\right]\sqrt{2}\,\mathrm{We}_s^{-1/2}. \tag{9}$$

Accounting for the infinite medium and self-similar stretching, the dispersion relation for the second phase is defined as

$$\tilde{\omega}_2^2 = \left(\frac{\tilde{k}}{\tilde{R}}\right)^3. \tag{10}$$

The initial conditions for phase 2 are the final conditions at the end of phase 1 where $f_2(\tilde{t}=0) = f_1(\tilde{t}=0)$ and $\dot{f}_2(\tilde{t}=0) = \dot{f}_1(\tilde{t}=0)$ [5]. Solving for $\ddot{f}_2 = -\tilde{\omega}_2{}^2 f_2(\tilde{t})$ produces

$$f_2(\tilde{t}) = \cos\left[\left(\frac{\tilde{k}}{\tilde{R}}\right)^{3/2}\tilde{t}\right] + \mathrm{We}_s^{1/2}\,\tilde{k}\left(\frac{\tilde{k}}{\tilde{R}}\right)^{-3/2}\sin\left[\left(\frac{\tilde{k}}{\tilde{R}}\right)^{3/2}\tilde{t}\right], \tag{11}$$

$$\dot{f}_2(\tilde{t}) = -\left(\frac{\tilde{k}}{\tilde{R}}\right)^{3/2}\sin\left[\left(\frac{\tilde{k}}{\tilde{R}}\right)^{3/2}\tilde{t}\right] + \mathrm{We}_s^{1/2}\,\tilde{k}\cos\left[\left(\frac{\tilde{k}}{\tilde{R}}\right)^{3/2}\tilde{t}\right]. \tag{12}$$

Using (11), (12), and (9), f_2 and $\dot{f}_2$ at the end of the second phase are written as functions of $\tilde{k}$ as

$$f_2(\tilde{t}_t) = \cos\left(\tilde{k}\sqrt{\frac{3}{4}}\tilde{t}_t\right) + \sqrt{\frac{4}{3}\mathrm{We}_s}\sin\left(\tilde{k}\sqrt{\frac{3}{4}}\tilde{t}_t\right), \tag{13}$$

$$\dot{f}_2(\tilde{t}_t) = -\tilde{k}\sqrt{\frac{3}{4}}\sin\left(\tilde{k}\sqrt{\frac{3}{4}}\tilde{t}_t\right) + \mathrm{We}_s^{1/2}\,\tilde{k}\cos\left(\tilde{k}\sqrt{\frac{3}{4}}\tilde{t}_t\right). \tag{14}$$

The third phase is characterized by the evolution of the wave mode on a thinning sheet until the amplitude of the mode is of the order of the sheet thickness. The mode that fulfills this condition for the shortest time is the breakup wave mode characterized by the breakup wave number $\tilde{k}_b$. This value is found computationally by substituting (9) into (14) and solving for

$$\dot{f}_2(\tilde{k}_b) \approx \max\left(\mathrm{We}_s^{1/2}\,\tilde{k}\cos\left\{\sqrt{\frac{3}{2}}\,\mathrm{We}_s^{-1/2}\,\tilde{k}\left[\left(\frac{4}{3}\tilde{k}\right)^{1/3} - 1\right]\right\}\right). \tag{15}$$

The thin sheet dispersion relation in the third phase, which includes self-similar stretching, is given as [5]

$$\tilde{\omega}_3^2 = \frac{\tilde{h}}{2}\left(\frac{\tilde{k}}{\tilde{R}}\right)^4. \tag{16}$$

The amplitude function in phase 3 can now be derived with the same general solution as phase 2 for $\ddot{f}_3 = -\tilde{\omega}_3^2 f_3$ as [5]

$$f_3(\tilde{t}) = f_2(\tilde{t}_t)\cos\left[\sqrt{\frac{\tilde{h}}{2}}\left(\frac{\tilde{k}}{\tilde{R}}\right)^2(\tilde{t}-\tilde{t}_t)\right] + \dot{f}_2(\tilde{t}_t)\sqrt{\frac{2}{\tilde{h}}}\left(\frac{\tilde{k}}{\tilde{R}}\right)^{-2}\sin\left[\sqrt{\frac{\tilde{h}}{2}}\left(\frac{\tilde{k}}{\tilde{R}}\right)^2(\tilde{t}-\tilde{t}_t)\right]. \tag{17}$$

Substituting (1), (2), (9), (13), and (14) and using the small angle approximation, this expression conveniently simplifies to

$$f_3(\tilde{t}) \approx \mathrm{We}_s^{1/2}\,\tilde{k}\tilde{t}. \tag{18}$$

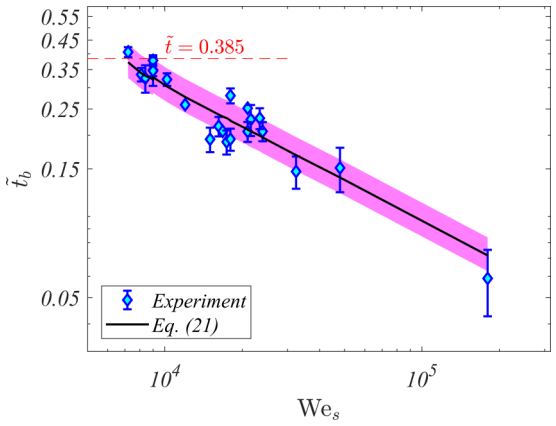

FIG. 6. The breakup time $\tilde{t}_b$ plotted as a function of We_s and compared with (21). Rupture of the sheet does not appear for $\tilde{t}_b \gtrapprox 0.385$, which corresponds to the time of the maximum rim radius. The highlighted area marks the variation in Eq. (21) for $\eta_0 = 60$–80 nm. The coefficient of determination for the logarithms of experimental values compared to Eq. (21) is $R^2 = 0.90$.

The time to the appearance of the first perforation $\tilde{t}_b$ is the time at which the amplitude of the fastest growing wave number $\tilde{k}_b$ is on the order of the sheet thickness.

There will be a contraction of the perturbation amplitude due to mass conservation resulting in $\tilde{\eta}_0/\tilde{k}^2 \sim \tilde{\eta}_{0,3}/(\tilde{k}/\tilde{R})^2$, where $\tilde{\eta}_{0,3}$ is the initial perturbation amplitude attenuated by self-similar stretching [18]. Using (1) and (2) an expression is found for the stretched perturbation amplitude in relation to the sheet thickness [6],

$$\frac{\tilde{\eta}_{0,3}}{\tilde{h}} = \frac{3}{4}\tilde{\eta}_0. \tag{19}$$

Substituting (19) into (3) gives the relation to solve for $\tilde{t}_b$,

$$\frac{\tilde{\eta}_{0,3}}{\tilde{h}} f_3(\tilde{k}_b, \tilde{t}_b) = \frac{3}{4}\tilde{\eta}_0 f_3(\tilde{k}_b, \tilde{t}_b) = 1. \tag{20}$$

Solving for $\tilde{t}_b$ reveals

$$\tilde{t}_b \approx \frac{4}{3}\tilde{\eta}_0^{-1}\tilde{k}_b^{-1}\,\mathrm{We}_s^{-1/2}. \tag{21}$$

In Fig. 6 the experimental $\tilde{t}_b$ was compared against (21) as a function of We_s where $\tilde{t}_b$ was measured for all test cases where hole perforation occurs and the droplet has not been drilled through. The initial wave amplitude was chosen to fit the data as $\eta_0 = 70$ nm, which is within the expected range of the ablation depth of $\eta_0 \sim 60$–80 nm highlighted in light purple in Fig. 6. It should be noted as well here that $\tilde{t}_b$ does not exceed $\sim$0.45 for any case, which is near the time of the maximum rim radius $\tilde{t} \sim 0.385$ according to (1) [12].

IV. CONCLUSIONS

Experiments were performed imaging sequences of shadowgraphs of droplets irradiated by bursts of picosecond laser pulses. A plethora of different deformation patterns were observed depending upon the burst parameters. Regardless of the burst parameters, the breakup dynamics are strongly coupled to the splash Weber number We_s, which describes the expansion of the droplet sheet rim radius until breakup. The experimental data support the claim of damping of the shorter wavelength hydrodynamic instabilities during the laser ablation induced droplet surface acceleration. Understanding these dynamics is necessary in the field of droplet target shaping in order to predict the maximum target surface size for the given laser parameters before disintegration. The derived Rayleigh-Taylor model would potentially allow the prediction of the perforation spacing λ_p using the breakup wave number as $\lambda_p = 2\pi\tilde{R}(\tilde{t}_b)r_0/\tilde{k}_b$. For the cases measured, the Mach number on the ablating droplet surface defined as $\mathrm{Ma} = P_s\rho^{-1}c_s^{-2}$, where P_s is the maximum ablation pressure, is $\mathrm{Ma} \ll 1$. Therefore, compressibility effects are neglected in this work. This provides a basis for predicting the fragment size distribution of the disintegrating sheet. The investigation of these fragment distributions will be presented in future work.

ACKNOWLEDGMENTS

The authors would like to thank the Swiss National Science Foundation for the generous grants (Grants No. 200021 156754 and No. 206021 164026) which funded this work. The authors would like to thank Flori Alickaj, Rolf Rüttimann, and Thomas Künzle for their support with the electrical and mechanical implementation, as well as Markus Brandstätter, Marco Weber, and the rest of the ALPS group members for the helpful discussions and their support.

[1] V. Bakshi, *EUV Lithography*, SPIE Press Monograph Vol. 178 (SPIE Wiley, Bellingham, WA, 2009).
[2] R. S. Abhari, B. Rollinger, A. Z. Giovannini, O. Morris, I. Henderson, and S. S. Ellwi, J. Micro/Nanolithogr., MEMS, MOEMS **11**, 021114 (2012).
[3] D. Hudgins, N. Gambino, B. Rollinger, and R. S. Abhari, J. Phys. D: Appl. Phys. **49**, 185205 (2016).
[4] Y. Ueno, T. Yanagida, T. Suganuma, H. Komori, A. Sumitani, and A. Endo, Proc. SPIE **7361**, 73610X (2009).
[5] N. Bremond and E. Villermaux, J. Fluid Mech. **524**, 121 (2005).
[6] A. L. Klein, Laser impact on flying drops, Ph.D. thesis, University of Twente, 2017.
[7] D. Kurilovich, T. de Faria Pinto, F. Torretti, R. Schupp, J. Scheers, A. S. Stodolna, H. Gelderblom, K. S. E. Eikema, S. Witte, W. Ubachs, R. Hoekstra, and O. O. Versolato, Phys. Rev. Appl. **10**, 054005 (2018).
[8] D. Hudgins and R. S. Abhari, U.S. Patent Application No. 16/128,545 (pending).
[9] N. Gambino, R. Abhari, F. Alickaj, F. Daners, A. Giovannini, O. Morris, and B. Rollinger, Method for controlling an interaction between droplet targets and a laser and apparatus for conducting said method, U.S. Patent No. 14/412,819 (2014).
[10] D. Hudgins and R. S. Abhari (unpublished).

[11] H. Gelderblom, H. Lhuissier, A. Klein, W. Bouwhuis, D. Lohse, E. Villermaux, and J. Snoeijer, J. Fluid Mech. **794**, 676 (2016).
[12] E. Villermaux and B. Bossa, J. Fluid Mech. **668**, 412 (2011).
[13] E. V. Rozhitsina, S. Gruner, I. Kaban, W. Hoyer, V. E. Sidorov, and P. S. Popel', Russ. Metall. (Engl. Transl.) **2011**, 118 (2011).
[14] S. Y. Grigoryev, B. V. Lakatosh, M. S. Krivokorytov, V. V. Zhakhovsky, S. A. Dyachkov, D. K. Ilnitsky, K. P. Migdal, N. A. Inogamov, A. Y. Vinokhodov, V. O. Kompanets, Y. V. Sidelnikov, V. M. Krivtsun, K. N. Koshelev, and V. V. Medvedev, Phys. Rev. Appl. **10**, 064009 (2018).
[15] C. Clanet and E. Villermaux, J. Fluid Mech. **462**, 307 (2002).
[16] A. J. Cole, J. D. Kilkenny, P. T. Rumsby, R. G. Evans, C. J. Hooker, and M. H. Key, Nature (London) **299**, 329 (1982).
[17] M. H. Emery, J. P. Dahlburg, and J. H. Gardner, Phys. Fluids **31**, 1007 (1988).
[18] S. T. Thoroddsen and J. Sakakibara, Phys. Fluids **10**, 1359 (1998).